

MOLECULAR GAS RESERVOIRS IN CLUSTER GALAXIES AT Z=1.46

MASAO HAYASHI¹, KEN-ICHI TADAKI¹, TADAYUKI KODAMA², KOTARO KOHNO^{3,4}, YUKI YAMAGUCHI³, BUNYO HATSUKADE³, YUSEI KOYAMA^{5,6}, RHYTHM SHIMAKAWA^{1,7}, YOICHI TAMURA⁸, TOMOKO L. SUZUKI¹

¹National Astronomical Observatory of Japan, Osawa, Mitaka, Tokyo 181-8588, Japan; masao.hayashi@nao.ac.jp

²Astronomical Institute, Tohoku University, Aramaki, Aoba-ku, Sendai 980-8578, Japan

³Institute of Astronomy, Graduate School of Science, The University of Tokyo, 2-21-1 Osawa, Mitaka, Tokyo 181-0015, Japan

⁴Research Center for the Early Universe, Graduate School of Science, The University of Tokyo, 7-3-1 Hongo, Bunkyo-ku, Tokyo 113-0033, Japan

⁵Subaru Telescope, National Astronomical Observatory of Japan, 650 North A'ohoku Place, Hilo, HI 96720, USA

⁶Department of Astronomical Science, SOKENDAI (The Graduate University for Advanced Studies), Mitaka, Tokyo 181-8588

⁷UCO/Lick Observatory, University of California, 1156 High Street, Santa Cruz, CA 95064, USA and

⁸Department of Physics, Nagoya University, Furo-cho, Chikusa-ku, Nagoya 464-8601, Japan

Draft version July 16, 2018

ABSTRACT

We present molecular gas reservoirs of eighteen galaxies associated with the XMMXCS J2215.9-1738 cluster at $z = 1.46$. From Band 7 and Band 3 data of the Atacama Large Millimeter/submillimeter Array (ALMA), we detect dust continuum emission at $870 \mu\text{m}$ and CO $J = 2-1$ emission line from 8 and 17 member galaxies respectively within a cluster-centric radius of R_{200} . The molecular gas masses derived from the CO and/or dust continuum luminosities show that the fraction of molecular gas mass and the depletion time scale for the cluster galaxies are larger than expected from the scaling relations of molecular gas on stellar mass and offset from the main sequence of star-forming galaxies in general fields. The galaxies closer to the cluster center in terms of both projected position and accretion phase seem to show a larger deviation from the scaling relations. We speculate that the environment of galaxy cluster helps feed the gas through inflow to the member galaxies and also reduce the efficiency of star formation. The stacked Band 3 spectrum of 12 quiescent galaxies with $M_{\text{stellar}} \sim 10^{11} M_{\odot}$ within $0.5R_{200}$ shows no detection of CO emission line, giving the upper limit of molecular gas mass and molecular gas fraction to be $\lesssim 10^{10} M_{\odot}$ and $\lesssim 10\%$, respectively. Therefore, the massive galaxies in the cluster core quench the star formation activity while consuming most of the gas reservoirs.

Subject headings: galaxies: clusters: individual (XMMXCS J2215.9-1738) — galaxies: ISM — galaxies: star formation — galaxies: high-redshift — galaxies: evolution

1. INTRODUCTION

Quiescent galaxies dominate galaxy clusters in the local Universe (e.g., Dressler et al. 1997; Peng et al. 2010; Scoville et al. 2013), which implies that the environment of galaxy clusters has an impact on the transition of star-forming galaxies to quiescent galaxies. Based on the Kennicutt–Schmidt relation (Schmidt 1959; Kennicutt 1998; Kennicutt & Evans 2012) demonstrating empirically that the gas content of galaxies is one of the most essential quantities that govern star-formation activities in galaxies, better understanding the evolution of galaxies in galaxy clusters in terms of both star-formation activity and gas content leads to identifying environmental processes responsible for quenching of star formation in galaxies.

Most of star-forming galaxies in the local Universe follow a tight positive correlation between star formation rate (SFR) and stellar mass which is called a main sequence of star-forming galaxies (e.g., Daddi et al. 2007; Elbaz et al. 2007; Noeske et al. 2007; Renzini & Peng 2015). Gas fraction and star formation efficiency of galaxies can be responsible for deviation from the main sequence in the plane of SFR- M_{stellar} , in the sense that starburst (passive) galaxies tend to have larger (smaller) gas fraction and/or higher (lower) efficiency of star formation (Saintonge et al. 2012, 2016, 2017; Sargent et al. 2014). On the other hand, as long as we focus on star-

forming galaxies, an environment where galaxies reside do not have a strong impact on the star-forming main sequence and the relationship between gas reservoirs and star-formation activity (Peng et al. 2010; Koyama et al. 2017). These observational studies may suggest that star formation activity in most of galaxies is governed not by external process such as galaxy interaction but by internal factors such as gas reservoir. However, since galaxies in the local clusters have already evolved, it is essential to investigate evolving cluster galaxies in the early Universe to reveal how the present-day quiescent galaxies quench the star formation within the galaxy clusters.

Observations in the high- z Universe have also been conducted actively and it is found that a main sequence of star-forming galaxies exists at each redshift up to $z \sim 3$ or higher (e.g., Speagle et al. 2014; Whitaker et al. 2014; Schreiber et al. 2015). Now that it becomes possible to compile about three orders of magnitude measurements of molecular gas from individual galaxies and stacks at $z = 0-4$, scaling relations of molecular gas fraction and depletion time scale on offset from the main sequence, i.e., stellar mass, SFR, and redshift, are constructed (Genzel et al. 2015; Tacconi et al. 2018; Scoville et al. 2017). The gas fraction of galaxies tend to be larger at higher redshifts (e.g., Tacconi et al. 2010, 2013; Geach et al. 2011; Saintonge et al. 2013; Scoville et al. 2017), as if it follows the redshift evolution of cosmic SFR density

(Madau & Dickinson 2014), suggesting that the SFR of a galaxy with a given mass becomes larger in proportion to the gas fraction as the redshift increases. In spite of the remarkable recent progress, most of the observations of molecular gas at high redshifts have been limited to the galaxies in general fields (e.g., Magnelli et al. 2012; Carilli & Walter 2013; Walter et al. 2014; Genzel et al. 2015; Silverman et al. 2015; Decarli et al. 2016a,b; Seko et al. 2016; Tacconi et al. 2018; Scoville et al. 2017). An increasing number of studies have surveyed molecular gas in galaxy (proto-)clusters at high redshifts of $z \approx 1-3$, however, the measurements of the gas content are at most for a few member galaxies in each cluster (Wagg et al. 2012; Aravena et al. 2012; Casasola et al. 2013; Ivison et al. 2013; Tadaki et al. 2014; Chapman et al. 2015; Wang et al. 2016; Dannerbauer et al. 2017; Noble et al. 2017; Rudnick et al. 2017; Stach et al. 2017; Lee et al. 2017; Webb et al. 2017).

XMMXCS J2215.9-1738 galaxy cluster at $z = 1.457$ ($22^{\text{h}}15^{\text{m}}58^{\text{s}}.5, -17^{\circ}38'02.5''$; Stanford et al. 2006) is one of the best targets to probe the early phase of environmental effects on molecular gas properties in cluster galaxies. This is because in addition to previous studies indicating that massive galaxies in the cluster core are still in their formation phase (Hayashi et al. 2010, 2014; Hilton et al. 2010; Ma et al. 2015), CO $J = 2-1$ ($\nu_{\text{rest}} = 230.538$ GHz, hereafter CO(2-1)) emission lines are found with ALMA from 17 galaxies associated with the galaxy cluster (Hayashi et al. 2017). Accretion phases of the gas-rich member galaxies are discussed based on the phase space of relative velocity versus cluster-centric distance. The galaxies with CO(2-1) detected disappear from the very center of the cluster, suggesting that the gas-rich galaxies have entered the cluster more recently than the gas-poor galaxies located in the virialized region of this cluster. Hayashi et al. (2017), for the first time, succeed in detecting CO(2-1) emission lines from as many as 17 member galaxies in the cluster at $z = 1.46$. Next step to better understanding of the evolution of cluster galaxies is to investigate their gas reservoirs and efficiency of star formation.

Stach et al. (2017) have independently detected fourteen 1.25mm dust continuum sources from their own ALMA data in the central region of the XMMXCS J2215.9-1738 cluster. Among them, the eleven sources are confirmed to be cluster members and the six sources have both CO(2-1) and CO(5-4) emission lines detected. The detections of dust continuum and/or CO line are consistent with those reported by Hayashi et al. (2017). The ratio of CO luminosities from the different transitions in the cluster is similar to those for field galaxies at similar redshifts. Gas masses of $\sim(1-2.5) \times 10^{10} M_{\odot}$ and a relatively short gas consumption timescale of ~ 200 Myr are estimated for the galaxies under assumption of a conversion factor of $\alpha_{\text{CO}} = 1$. They argue that based on the line widths and luminosities of the two CO transitions, the CO(2-1) gas tends to be stripped from the galaxies rather than the CO(5-4) gas, which implies an environmental process acts on the cluster galaxies.

In this paper, we present full discussions from our ALMA observations in Band 3 and Band 7 in the XMMXCS J2215.9-1738 galaxy cluster through two programs of 2015.1.00779.S and 2012.1.00623.S. The data in Band 3 and Band 7 allow us to detect CO(2-1) emis-

sion and dust continuum emission at $870 \mu\text{m}$ from cluster member galaxies, respectively. We use the ALMA data to investigate molecular gas reservoirs in the member galaxies and then discuss the evolution of their star formation activities in terms of star formation efficiency and gas consumption. The outline of this paper is as follows. In Section 2, the ALMA data as well as ancillary data covering optical to mid-infrared (MIR) are described. The source detection in the ALMA Band 7 data is performed and the photometric catalog with multi-band photometry is created. In Section 3, we derive molecular gas mass from the ALMA data, and discuss fraction of molecular gas mass and depletion time scale for the cluster member galaxies in the central region. In Section 4, we compare our results with the scaling relation for field galaxies and results of other clusters at $z \sim 1.6$ from literature. We also discuss the molecular gas mass in quiescent galaxies in the very center by stacking the Band 3 data. Conclusions are shown in Section 5. Throughout the paper, the cosmological parameters of $H_0 = 70 \text{ km s}^{-1} \text{ Mpc}^{-1}$, $\Omega_m = 0.3$, and $\Omega_{\Lambda} = 0.7$, along with Chabrier (2003) initial mass function (IMF), are adopted. The velocity dispersion of the cluster member galaxies is $\sigma = 720 \text{ km s}^{-1}$ and the radius of the galaxy cluster is $R_{200} = 0.8 \text{ Mpc}$ (Hilton et al. 2010).

2. DATA

2.1. ALMA Band 3

Hayashi et al. (2017) already report the initial results from the Band 3 data. Since the details of the Band 3 data and source detection in the data are described in the paper, we briefly mention them in this section.

The Band 3 data are available in 2.33 arcmin^2 observed at three pointings, where an area within $0.5 R_{200}$ from the cluster center is almost covered. The spectral coverage is $93.03 - 94.86 \text{ GHz}$ with a spectral resolution of 13.906 MHz ($\sim 12.5 \text{ km s}^{-1}$). Integration time is 1.04 hours per each pointing. Typical noise level of the mosaicked 3D cubes is $0.12 \text{ mJy beam}^{-1}$ at velocity resolutions of 400 km s^{-1} . The synthesized beam size is $1.79'' \times 1.41''$.

We use Clumpfind (Williams et al. 1994) to search for emission lines on the data cube. The emission-line search is performed in the cubes with different velocity resolutions of $50, 100, 200, 400,$ and 600 km s^{-1} . We have detected 21 candidates at signal-to-noise ratio (SNR) of > 5.0 in at least one velocity resolution, after excluding overlaps. We cross-match the detections in the ALMA data with the optical and near-infrared (NIR) data described in § 2.3 to remove the possible false detections. Consequently, we conclude that 17 emission lines with counterparts in the optical-NIR data are secure detections. The spectroscopic redshifts (if any), photometric information such as colors are fully consistent with the counterparts being the member galaxies. Note that the remaining four candidates are not detected in the 1.25mm dust continuum data in ALMA Band 6 shown by Stach et al. (2017) and our ALMA Band 7 data described below are not available to them. The spectra, the intensity maps, and the properties of the individual 17 emission lines are shown in Hayashi et al. (2017). For cluster member galaxies without individual CO detection (§ 2.4), we estimate an upper limit of CO luminosity from

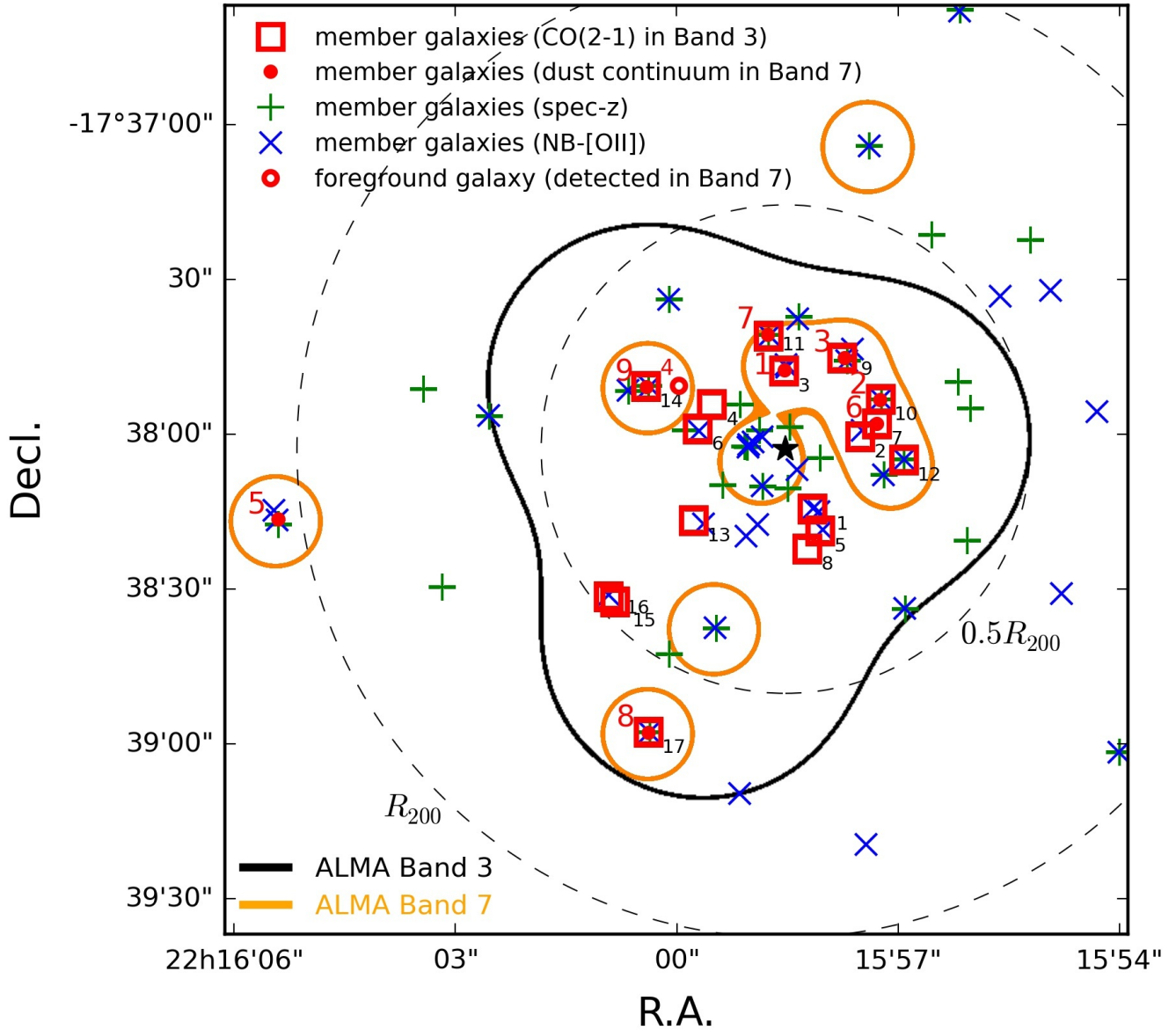


FIG. 1.— Spatial distribution of galaxies detected in the ALMA data. Filled red circles show the cluster member galaxies with dust continuum detected in Band 7. Open red circle also shows a Band 7 source, but it is a foreground galaxy at $z = 1.30$ (Stach et al. 2017). Open squares show the member galaxies with detection of CO(2-1) emission line. The numbers next to the symbols are IDs shown in Tables 1 and 2. The black (orange) curves show the area where Band 3 (7) data are available. The green and blue crosses show the member galaxies confirmed by spectroscopy and [O II] emitters associated with the cluster, respectively (Hilton et al. 2010; Beifiori et al. 2017; Hayashi et al. 2014). A star symbol shows a cluster center determined with extended X-ray emission (Stanford et al. 2006). The dashed circles show the cluster-centric radius of $0.5R_{200}$ and R_{200} (Hilton et al. 2010).

5σ noise level in the cube with 400 km s^{-1} velocity resolution.

2.2. ALMA Band 7

The observations in Band 7 were conducted in 2015 July. Four spectral windows are set at central frequencies of 338, 340, 350 and 352 GHz with each bandwidth of 1.875 GHz, respectively. The data are taken at ten pointings to target 13 [O II] emission-line galaxies (Hayashi et al. 2010) that have dust-corrected $\text{SFR}_{[\text{O II}]}$ of $> 93 M_{\odot} \text{ yr}^{-1}$, which results in the patchy data coverage of 0.61 arcmin^2 (Figure 1). Integration time is 7.06 minutes

per each pointing. The synthesized beam size is $0.181'' \times 0.157''$ with a position angle of 44.7 degrees. The spatial resolution is comparable to optical – NIR data observed with Hubble Space Telescope (HST).

Calibration of the raw data is conducted using the Common Astronomy Software Applications (CASA version 4.3.1; McMullin et al. 2007) with a standard ALMA pipeline. The Briggs weighting with the robust parameter of 2.0 (i.e., natural weighting) and a CLEAN threshold of 0.35 mJy ($\sim 5\sigma$) are adopted to make CLEANed images. Among ten pointings, the data at five pointings nearest from the cluster center are mosaiced to make a single image (Figure 1). Typical noise levels of these im-

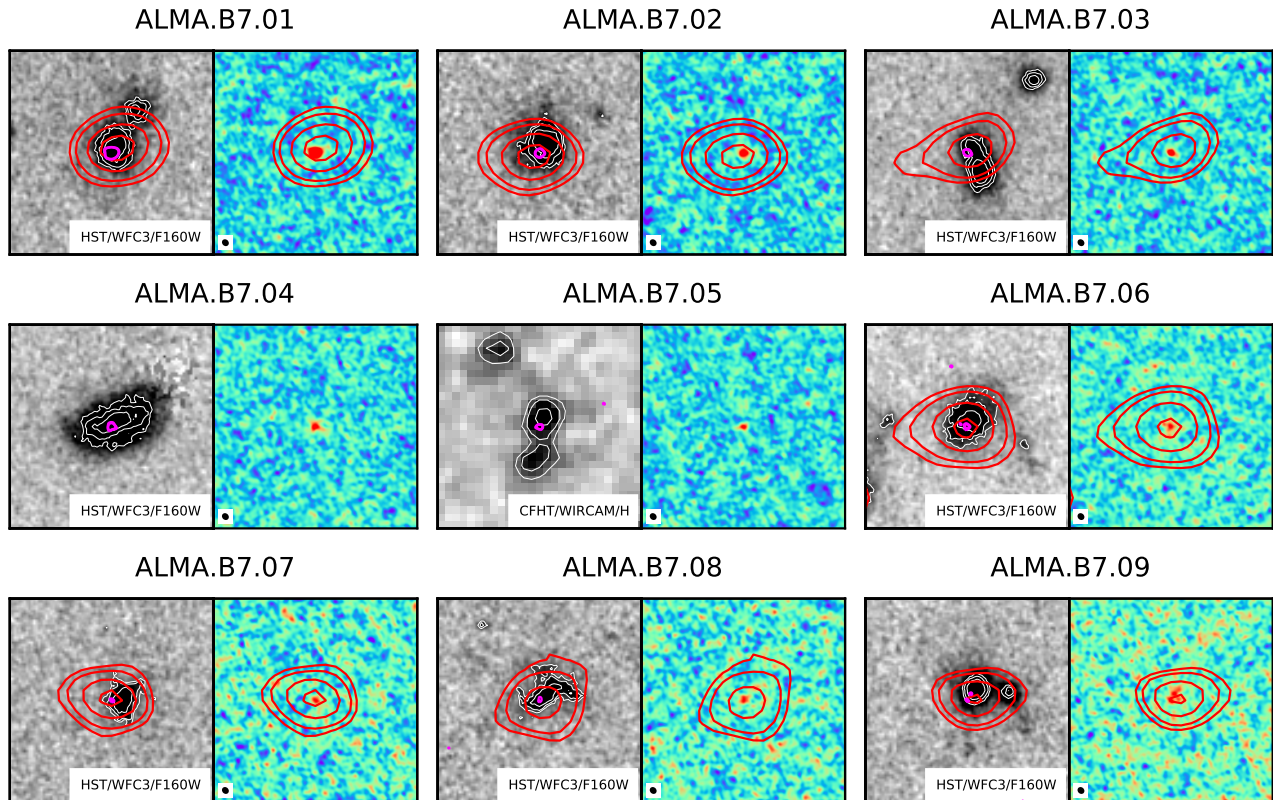


FIG. 2.— Postage-stamps of the galaxies detected in ALMA Band 7, where 5 arcsec on a side. The right panel shows the intensity map in Band 7, and the synthesized beam size is shown in black in the lower left corner. The left panel shows the H -band image (HST/WFC3 F160W data if available, otherwise CFHT/WIRCam H -band) along with the white contours showing the Band 7 intensity map of 4.0σ , 4.5σ , and 5.0σ levels. The red contours in both panels show the intensity of CO(2–1) emission lines (Hayashi et al. 2017). Note that the ALMA.B7.04 is not a cluster member galaxy but a foreground galaxy (Table 1).

ages are $0.061 - 0.068$ mJy beam $^{-1}$, which are measured by fitting a Gaussian to the histogram of pixel counts while ignoring the bright end of the histogram that some bright sources can contribute to.

We search for sources with a pixel count larger than 4.6σ in each image. We have detected 9 sources at $870\mu\text{m}$ from the Band 7 data, all of which have a counterpart in optical and NIR data (Figure 2). Similar to the 1.25mm dust continuum sources reported by Stach et al. (2017), Figure 2 suggests that the several $870\mu\text{m}$ dust continuum sources have an adjacent companion of smaller object. The detection threshold lower than 4.6σ results in selecting sources without any counterpart in optical and NIR data, and thus they are likely to be spurious sources. This suggests that the threshold that we apply is reasonable. As another check of the reliability of the extracted sources, we also apply the same threshold to the inverted data to select pixels with a large negative value and then find only one negative detection. Therefore, we conclude that all of the detections are real (Table 1).

The flux densities of the dust continuum emission are measured with a $0.44''$ ($=22$ pixels)-diameter aperture, i.e., $\sim 2.4\times$ the beam size. The error of the flux densities are estimated from the 10,000 measurements with the same aperture at the random positions over the individual images. The 1σ error is derived by fitting a Gaussian to the histogram of the random measurements.

We also measure the flux densities in the uv-tapered map with the synthesized beam size of $0.48'' \times 0.46''$ to verify whether there is a flux of an extended component resolved out. The photometry is performed in the same manner as in the natural weighting map, but for the $1.0''$ -diameter aperture being used for the measurement in the tapered map. In the case that the measurement in the natural weighting map is consistent with that in the tapered map within the 1σ error, we use the flux densities measured in the natural weighting map. Otherwise, we use the measurement in the uv-tapered map. The flux densities measured are shown in Table 1.

The 9 detections with $S_{\nu,870\mu\text{m}} > 0.49$ mJy in 0.61 arcmin 2 suggests that the number density of the $870\mu\text{m}$ sources in this region is a factor of 2–3 larger than expected from the cumulative number counts of ALMA dust continuum sources in deep general fields (e.g., Fujimoto et al. 2016; Hatsukade et al. 2016). However, since the patchy coverage of the ALMA Band 7 data does not cover the region where there are many cluster members, the number density would be a lower limit. Indeed, Stach et al. (2017) report that the center of this cluster is a $\sim 7\times$ overdensity of 1.25mm dust continuum sources.

Seven out of the nine sources have a counterpart of CO(2–1) emitters detected in the Band 3 data (Figure 2). Comparing the intensity map of CO(2–1) with the map of Band 7, the position of both dust continuum and CO

emission coincides well. Also, the dust continuum emission comes from the compact region of the center of the individual galaxy, which is similar to the previous studies for high- z galaxies (Simpson et al. 2015; Ikarashi et al. 2015; Barro et al. 2016; Hodge et al. 2016; Tadaki et al. 2017; Chen et al. 2017). Although one source, B7.05, is located out of the Band 3 data coverage, it has a counterpart of [O II] emitters selected by Subaru/Suprime-Cam narrowband imaging (Hayashi et al. 2014). However, the source B7.04 is likely to be a foreground galaxy judging from the appearance in the optical and NIR data (see also Stach et al. 2017, which show that this is a galaxy at $z = 1.30$). Therefore, we regard the eight $870\mu\text{m}$ sources as the cluster member galaxies. Combining the results of Hayashi et al. (2017), we have found 18 detections in total in the ALMA Band 3 and Band 7 data (see Figure 1 and Table 2).

2.3. Archival imaging data

We have optical images taken with Subaru/Suprime-Cam in B, R_c, i', z' , NB912 and NB921, which are used in our previous studies (e.g., Hayashi et al. 2010, 2014). Other imaging data in optical to infrared (IR) wavelengths are retrieved from public archive. The Canada-France-Hawaii Telescope Legacy Deep Survey (CFHTLS-Deep) provides us with the complementary optical images taken with CFHT/MegaCam in u^* and g' , and the WIRCam Deep Survey (WIRDS, Bielby et al. 2012) provides us with the NIR images taken with CFHT/WIRCam in J, H and K_s , all of which are retrieved from the CFHT Science Archive. Other NIR images taken with a Wide Field Camera 3 (WFC3) on HST in F125W, F140W, and F160W filters (Beifiori et al. 2017) are also retrieved from the HST archive. MIR data of Spitzer/IRAC 3.6–5.8 μm and MIPS 24 μm (Hilton et al. 2010) are retrieved from the Spitzer Heritage Archive (SHA). We do not use IRAC 8.0 μm data because the data is not deep and thus many cluster members seem not to be detected in 8.0 μm .

A coadd image in MIPS 24 μm is created by ourselves from the Basic Calibrated Data (BCD) products retrieved from the archive. This is because some pixels suffer from soft saturation in the individual BCD products (see Hilton et al. (2010) for the details) and thus the image quality at the north side is not good in the MIPS 24 μm image reduced by the standard pipeline which can be retrieved from the archive. Therefore, we mask the regions suffering from soft saturation in the individual frames and then coadd them with MOPEX (MOsaicker and Point source EXtractor). Also, the pixel scale is set to be 1.25 arcsec per pixel.

2.4. Catalogs of cluster member galaxies

In addition to the sample of the 18 ALMA sources, we have other catalogs of cluster member galaxies selected from the previous studies (Hilton et al. 2010; Beifiori et al. 2017; Hayashi et al. 2010, 2011, 2014). The catalogs consist of [O II] emission-line galaxies selected from imaging with two narrowband filters (Hayashi et al. 2010,

2014) and galaxies confirmed by optical and NIR follow-up spectroscopy (Hilton et al. 2010; Hayashi et al. 2011, 2014; Beifiori et al. 2017). The catalogs provide us with additional 47 member galaxies within a radius of $1.1 \times R_{200}$ (Figure 1), where there are 31 [O II] emission-line galaxies and 32 spectroscopically confirmed galaxies. Note that the 16 galaxies in the sample of [O II] emitters overlap with those in the sample of spectroscopically confirmed galaxies. Therefore, we can use the sample of 65 cluster member galaxies within a cluster-centric radius of $\sim R_{200}$ in this study. The spatial distribution of the member galaxies is shown in Figure 1.

2.4.1. multi-band photometry

Photometry in the optical, NIR and MIR data is conducted for the ALMA sources as well as the other cluster member galaxies. SExtractor (Bertin & Arnouts 1996) is used for photometry in the optical, NIR and IRAC data. Since the seeing of the Subaru images is 1.09 arcsec which is worse than the other images (Hayashi et al. 2014), we match the point spread function (PSF) between the optical and NIR images. Note that we do not match the PSF of the IRAC images. This is because the PSF of IRAC data is quite different from the optical or NIR data and thus it is not advisable to match the PSF of optical and NIR data to that of IRAC data. We run SExtractor in double image mode. The H -band images with better seeing before the PSF is matched, i.e., WFC3/F160W if available, otherwise WIRCam/ H , is used as a detection image. For the photometry in the optical and NIR data, we measure magnitudes of the galaxies with a 2''-diameter aperture and correct them for the aperture correction by 0.43 mag which is estimated from growth curve of a PSF to derive total magnitudes. The magnitudes are also corrected for the Galactic absorption assuming the extinction law of Cardelli et al. (1989). For the photometry in the IRAC data, magnitudes are measured with a 3''-diameter aperture, and then we apply the aperture correction of 0.54, 0.63, and 0.83 mag in [3.6], [4.5], and [5.8] to estimate the total magnitude.

We conduct PSF-fitted photometry with IRAF/DAOPHOT in the MIPS data, according to the previous studies (e.g., Magnelli et al. 2009). We use the IRAC 3.6 μm data as a reference image. We fit the PSF to the MIPS data in each position of IRAC 3.6 μm sources, and measure the flux in 24 μm . We check the residual image to make sure that the fitting works well. We apply the aperture correction of 0.53 mag which are estimated from growth curve of a PSF. To combine the photometry in the MIPS data with that in the shorter wavelengths, an aperture with a 1.5'' radius is used for the source matching. Seven of the 18 ALMA sources are detected in 24 μm (Table 2).

2.4.2. stellar mass, SFR, and rest-frame colors

The multi-band photometry covering the optical to MIR wavelengths is used to estimate stellar masses and SFRs of the galaxies. We use the C++ version¹ of FAST code (Kriek et al. 2009) to perform the spectral energy distribution (SED) fitting. The redshifts of the galax-

¹ <https://github.com/cschreib/fastpp>

TABLE 1
PROPERTIES OF GALAXIES DETECTED IN ALMA BAND 7

ID	R.A. (J2000)	Decl. (J2000)	S/N ^a	$S_{\nu,870\mu\text{m}}$ (mJy)	Detection ^b in 1.25mm	Counterpart
ALMA.B7.01	22 15 58.53	-17 37 47.6	17.4	2.58 ± 0.23^c	o (3)	NB921 [O II]
ALMA.B7.02	22 15 57.24	-17 37 53.4	10.2	1.08 ± 0.13	o (6)	NB912+NB921 [O II]
ALMA.B7.03	22 15 57.72	-17 37 45.2	10.0	0.71 ± 0.13	...	NB912+NB921 [O II]
ALMA.B7.04	22 15 59.97	-17 37 50.6	7.4	1.27 ± 0.18	o (4)	foreground galaxy ($z = 1.30$) ^d
ALMA.B7.05	22 16 05.40	-17 38 16.5	7.1	0.49 ± 0.14	—	NB912+NB921 [O II]
ALMA.B7.06	22 15 57.29	-17 37 58.0	6.1	1.12 ± 0.23^c	o (7)	sBzK
ALMA.B7.07	22 15 58.77	-17 37 40.8	4.8	0.70 ± 0.20	o (1)	NB912+NB921 [O II]
ALMA.B7.08	22 16 00.38	-17 38 57.9	4.7	0.51 ± 0.14	—	NB912+NB921 [O II]
ALMA.B7.09	22 16 00.40	-17 37 50.8	4.7	1.05 ± 0.24^c	o (5)	NB912 [O II]

^a The signal-to-noise ratio in source detection.

^b The numbers within parentheses show ID of the 1.25mm sources detected with ALMA Band 6 data by [Stach et al. \(2017\)](#). The “...” means non-detection in the data, while the “—” means that the data are not available for the galaxy.

^c The uv-tapered map is used for the measurement of flux density. See the text for the details.

^d The redshift is from [Stach et al. \(2017\)](#).

TABLE 2
PROPERTIES OF THE 18 GALAXIES DETECTED IN ALMA BAND 3 AND BAND 7

ID ^a	(B3)	(B7)	Redshift ^b	Star-forming or Quiescent ^c	M_{stellar} ($10^{10}M_{\odot}$)	$\text{SFR}_{\text{SED-fit}}$ ($M_{\odot} \text{ yr}^{-1}$)	$f_{\nu,24\mu\text{m}}$ (μJy)	$\text{SFR}_{\text{UV}+24\mu\text{m}}$ ($M_{\odot} \text{ yr}^{-1}$)	$M_{\text{gas,CO}}$ ($10^{10}M_{\odot}$)	$M_{\text{gas,dust}}$ ($10^{10}M_{\odot}$)
ALMA.01	01	—	1.466	S	$8.13^{+0.78}_{-0.54}$	35^{+35}_{-2}	125 ± 10	91^{+7}_{-8}	$10.5^{+0.5}_{-0.7}$	—
ALMA.02	02	...	1.450	S	$3.39^{+0.69}_{-0.57}$	31^{+15}_{-13}	$2.7^{+0.6}_{-0.6}$	<3.7
ALMA.03	03	01	1.453	S	$11.22^{+0.26}_{-1.22}$	25^{+21}_{-6}	$10.7^{+0.8}_{-0.5}$	$13.8^{+1.0}_{-1.2}$
ALMA.04	04	—	1.466	S	$3.89^{+1.01}_{-0.65}$	$6^{+2.8}_{-2.9}$	$3.7^{+0.6}_{-0.7}$	—
ALMA.05	05	—	1.467	S	$2.29^{+0.66}_{-0.39}$	48^{+26}_{-20}	$3.1^{+0.6}_{-0.7}$	—
ALMA.06	06	—	1.467	S	$12.02^{+2.33}_{-0.80}$	145^{+69}_{-32}	180 ± 11	129^{+9}_{-6}	$10.5^{+0.7}_{-0.5}$	—
ALMA.07	07	06	1.452	S	$8.13^{+0.19}_{-0.72}$	35^{+49}_{-0}	$5.8^{+0.6}_{-0.6}$	$6.2^{+1.2}_{-1.3}$
ALMA.08	08	—	1.457	S	$5.75^{+0.27}_{-0.63}$	105^{+30}_{-34}	88 ± 10	65^{+8}_{-7}	$6.8^{+0.5}_{-0.6}$	—
ALMA.09	09	03	1.468	S	$10.72^{+0.25}_{-1.17}$	47^{+27}_{-24}	$3.5^{+0.5}_{-0.5}$	$3.8^{+0.7}_{-0.8}$
ALMA.10	10	02	1.454	S	$3.98^{+0.28}_{-0.43}$	72^{+28}_{-12}	125 ± 10	91^{+7}_{-8}	$8.1^{+0.6}_{-0.5}$	$6.8^{+0.8}_{-0.9}$
ALMA.11	11	07	1.451	S	$1.82^{+0.33}_{-0.75}$	17^{+29}_{-5}	$6.6^{+0.8}_{-0.9}$	$5.1^{+1.3}_{-1.4}$
ALMA.12	12	...	1.445	S	$1.48^{+0.22}_{-0.10}$	54^{+15}_{-11}	71 ± 10	58^{+7}_{-6}	$4.1^{+0.6}_{-0.5}$	<4.6
ALMA.13	13	—	1.471	S	$6.03^{+0.43}_{-2.71}$	21^{+55}_{-3}	60 ± 10	44^{+8}_{-6}	$5.8^{+0.7}_{-0.6}$	—
ALMA.14	14	09	1.451	Q	$9.12^{+0.00}_{-1.88}$	$3^{+0.1}_{-2.5}$	$3.2^{+0.6}_{-0.6}$	$5.8^{+1.3}_{-1.3}$
ALMA.15	15	—	1.465	S	$3.63^{+1.74}_{-0.24}$	28^{+10}_{-18}	85 ± 11	62^{+8}_{-9}	$6.6^{+0.6}_{-0.9}$	—
ALMA.16	16	—	1.465	S	$3.09^{+0.30}_{-0.52}$	37^{+29}_{-11}	$8.5^{+0.6}_{-0.9}$	—
ALMA.17	17	08	1.460	S	$2.45^{+1.81}_{-0.46}$	123^{+51}_{-80}	$5.8^{+0.7}_{-0.6}$	$3.5^{+1.0}_{-1.0}$
ALMA.18	—	05	1.465	S	$2.51^{+0.80}_{-0.11}$	72^{+15}_{-35}	—	$3.4^{+1.0}_{-0.9}$

^a The “...” means non-detection in the data, while the “—” means that the data are not available for the galaxy (See Figure 1).

^b The redshifts are derived from the CO emission lines for all but ALMA.18 ([Hayashi et al. 2017](#)). The redshift of ALMA.18 is from [Hilton et al. \(2010\)](#).

^c The galaxies are classified as star-forming (S) or quiescent (Q) galaxies based on the rest-frame U-V and V-J colors (Figure 4).

ies are fixed at ones estimated from CO(2–1) lines, optical and NIR spectroscopy, and narrowband response functions, where the redshifts determined from the former have higher priority when the redshifts from several methods are available. The model SED templates of galaxies are generated by the code of [Bruzual & Charlot \(2003\)](#). Star formation histories of the exponentially declining model are adopted, where we set an e-folding time of $\log(\tau/\text{yr}) = 8.5\text{--}10.0$ with $\Delta \log(\tau/\text{yr}) = 0.1$ ([Wuyts et al. 2011](#)). The ages of 0.1–10.0 Gyr are acceptable with a step of $\Delta \log(\text{age}/\text{yr}) = 0.1$. The extinction curve of [Calzetti et al. \(2000\)](#) is assumed and A_V ranges from 0.0 to 3.0. Metallicity is fixed to the solar value. Monte Carlo simulation is performed 100 times for each galaxy

to estimate a 1σ error in stellar mass and SFR.

The intrinsic SFRs estimated are sensitive to reliability of correction for dust extinction. MIR data are useful to estimate a component of SFR obscured by dust, which suggests that it is not easy to estimate the dust obscured SFR from the rest-frame UV and optical data ([Tadaki et al. 2017](#); [Whitaker et al. 2017](#)). Several studies in a galaxy cluster at $z \sim 0.4$ suggest that galaxies in higher density regions tend to be more dusty ([Koyama et al. 2013](#); [Sobral et al. 2016](#)). Therefore, if a galaxy has a detection in $24 \mu\text{m}$, we estimate the SFR from the combination of UV and IR luminosities. Otherwise, we use the dust-corrected SFR derived from the SED fitting described above. The IR luminosities are estimated from 24

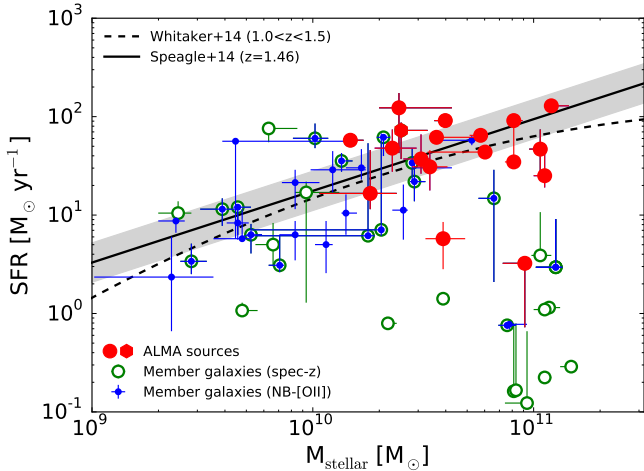


FIG. 3.— SFRs as a function of stellar mass for the cluster member galaxies within a radius of $\sim R_{200}$. The red symbols show the 18 ALMA sources: 17 CO(2–1) emitters are shown by circle, while the dust continuum source is shown by hexagon. The spectroscopically confirmed galaxies are shown by green circles and the [O II] emitters are shown by blue circles. The solid line with the gray region shows the main sequence with ± 0.2 dex given by Speagle et al. (2014), and the dashed line shows the one by Whitaker et al. (2014).

μm fluxes using a conversion factor given by Wuyts et al. (2008), and the UV luminosities are estimated from the rest-frame 2800 Å luminosity of the best-fit SED. Then, using the equation given by Wuyts et al. (2011),

$$\frac{\text{SFR}_{\text{UV+IR}}}{M_{\odot} \text{ yr}^{-1}} = 1.09 \cdot 10^{-10} \cdot \frac{L_{\text{IR}} + 3.3L_{2800}}{L_{\odot}}, \quad (1)$$

the UV+IR luminosities are converted to $\text{SFR}_{\text{UV+IR}}$.

Table 2 lists the stellar masses and SFRs for the ALMA sources. Figure 3 shows the SFRs of the galaxies as a function of stellar mass. We also plot the main sequence at redshift of $z \sim 1.46$ from the literature (Whitaker et al. 2014; Speagle et al. 2014). Most of the galaxies detected in ALMA data are located on or above the main sequence (MS) at the redshift (i.e., within ± 0.2 dex or higher from the MS). The other ALMA sources below the main sequence are massive galaxies with $\gtrsim 10^{10.6} M_{\odot}$.

Figure 4 shows the rest-frame U-V versus V-J colors of the member galaxies. The U-V and V-J colors are derived from the best-fit SED. According to Brammer et al. (2011), we use the response function of U and V filters defined by Maíz Apellániz (2006) and 2MASS-J filter to calculate the colors. The UVJ diagram is widely used to distinguish quiescent galaxies from star-forming galaxies (e.g., Labbé et al. 2005; Williams et al. 2009). Almost all of the CO(2–1) lines and dust continuum emissions are detected from star-forming galaxies. Along the sequence of the star-forming galaxies in the UVJ diagram, the ALMA sources tend to have redder colors, implying that the CO line and dust continuum emission are easier to be detected from more dusty star-forming galaxies (e.g., Tadaki et al. 2015; Rudnick et al. 2017). On the other hand, few quiescent member galaxies have either CO line or dust continuum emission detected. Indeed, the ALMA.14 is only classified as a quiescent galaxy (see also Table 2).

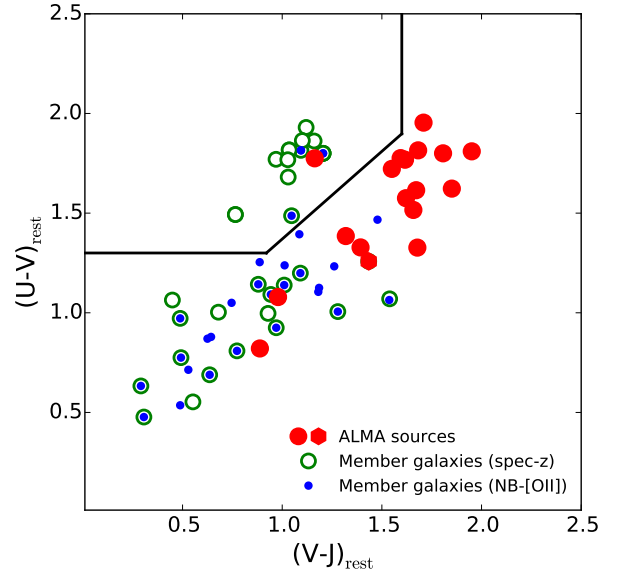


FIG. 4.— U-V versus V-J colors in the rest-frame. The symbols are the same as Figure 3. The solid line is a boundary to distinguish quiescent galaxies from star-forming galaxies (Williams et al. 2009).

3. RESULTS

3.1. molecular gas mass

We estimate molecular gas mass from luminosities of CO(2–1) emission line and dust continuum emission for the 18 cluster member galaxies with detection in ALMA data. The CO(2–1) luminosities are derived in Hayashi et al. (2017) from the intensity map integrated in velocity by the width of emission line ($2 \times \text{FWHM}$). The luminosity, $L'_{\text{CO}(2-1)}$, ranges $(4.5-22) \times 10^9 \text{ K km}^{-1} \text{ pc}^2$. The conversion factor from the CO luminosity to the molecular gas mass given by Tacconi et al. (2018) is adopted to estimate the molecular gas mass. We use $L'_{\text{CO}(1-0)}/L'_{\text{CO}(2-1)} = 1.2$ and $\alpha_{\text{CO}(1-0)} = 4.36$. Note that the conversion factor is corrected for the metallicity dependence through the stellar mass – metallicity relation (Genzel et al. 2012; Bolatto et al. 2013) and thus the conversion factors that we adopt range from 4.99 to 7.31 which are dependent on the stellar mass. We also use the equation (16) of Scoville et al. (2016) to estimate molecular gas mass from dust continuum emission at $870 \mu\text{m}$, where the dust temperature of $T_d = 25 \text{ K}$ is assumed and the metallicity (i.e., stellar mass)-dependent ratio of molecular gas to dust mass is taken into account according to Tacconi et al. (2018).

Figure 5 compares the molecular gas mass from CO(2–1) luminosity with that from dust continuum luminosity for galaxies with a detection in both CO and dust continuum. The molecular gas masses estimated from the two ways are consistent. Among the galaxies with CO(2–1) line in the area covered by ALMA Band 7 data, two CO(2–1) emitters are not detected in Band 7 (The IDs are ALMA.02 and ALMA.12). The two galaxies have the lowest CO(2–1) luminosities among the galaxies for which the Band 7 data are available. The 3.8σ source is seen in the Band 7 data near the position of ALMA.02,

while no source at more than 3σ is seen around the ALMA.12 within the synthesized beam of Band 3 data. We plot their upper limit of the molecular gas mass from dust continuum in Figure 5, suggesting that the gas mass from CO is not discrepant with the upper limit from dust continuum for the two galaxies. Hereafter, if the galaxies have CO luminosity available, we use the gas mass derived from CO. Otherwise, we use the gas mass derived from dust continuum, namely we use $M_{\text{gas,dust}}$ for the galaxy of ALMA.18 only. The molecular gas masses derived here are listed in Table 2. Moreover, we estimate an upper limit of the molecular gas mass from the upper limit of the CO luminosity (§ 2.1) for the individual member galaxies in the area covered by the Band 3 data.

The conversion factor applied to derive molecular gas mass from CO luminosity is one of the major uncertainties in the measurement. It is not obvious which conversion factors should be used. Stach et al. (2017) argue that at least two member galaxies in this cluster prefer the conversion factor $\alpha_{\text{CO}} = 1$ based on the comparison between gas mass from the CO luminosity and dynamical mass from the width of CO line. However, we find that the gas masses we estimate by the different ways, i.e. CO and dust continuum, are consistent with each other even for the two galaxies (ALMA.07 and ALMA.10 in Table 2). Moreover, we compare our results with the scaling relation for field galaxies given by Tacconi et al. (2018) in Section 4. The conversion factors that we apply in this work are the same as in Tacconi et al. (2018), which enables a fair comparison of our results with the scaling relation.

Figure 6 shows the SFRs of the member galaxies as a function of molecular gas mass. There may be a mild trend that galaxies with larger gas masses have larger SFRs, although larger sample is required for confirmation of this trend. At a given molecular gas, the galaxies can have a wide range of SFRs (~ 1.0 dex), indicating a wide range of star formation efficiency among the cluster member galaxies. The PHIBSS survey shows larger SFRs with ~ 0.5 dex dispersion at a given molecular gas for field galaxies at $z = 1.0$ –2.5 (Tacconi et al. 2013). These suggest that besides molecular gas, other factors also have an impact on the star formation activity of cluster galaxies.

3.2. Gas mass fraction and depletion time scale

Fraction of molecular gas mass to the sum of stellar and gas mass, $f_{\text{gas}} = M_{\text{gas}}/(M_{\text{gas}} + M_{\text{stellar}})$, and depletion time scale, $\tau = M_{\text{gas}}/\text{SFR}$, are useful to characterize evolutionary phases of the galaxies. The fraction of gas mass can imply how the member galaxies have gas reservoirs and then can proceed to form stars, and the depletion time is a time scale reflecting the efficiency of star formation in the galaxies. Since we expect that star-forming galaxies located in the central region of the cluster are good candidates of present-day massive early-type galaxies, it is important to investigate the fraction of gas mass and the depletion time scale for the member galaxies to discuss the evolution of the cluster galaxies.

We investigate how the gas fraction and the depletion time are related with the evolution of cluster galaxies. We here focus on the following four factors: stellar mass, offset from the MS of star-forming galaxies, cluster-centric radius, and accretion phase based on phase-space.

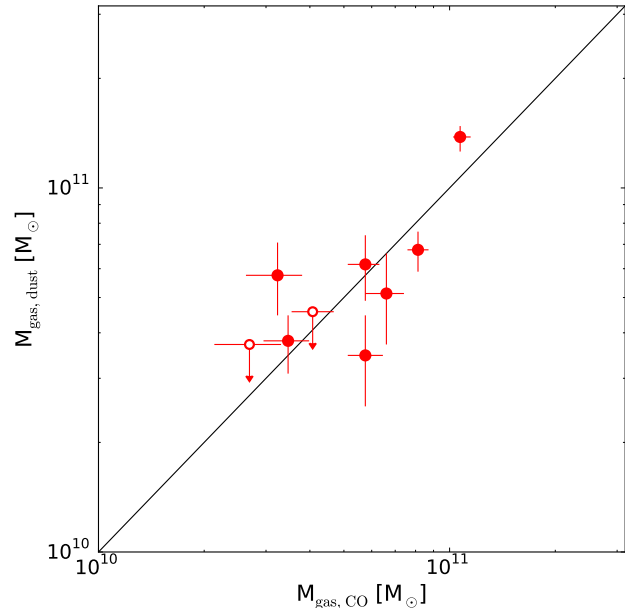


FIG. 5.— Comparison between molecular gas estimated from CO(2–1) and that from dust continuum for galaxies in the area where both Band 3 and Band 7 data are available. The filled circles show the cluster members with both CO(2–1) line and dust continuum detected. The open circles show the members with CO(2–1) lines detected but dust continuum not detected. The upper limits are estimated from the flux densities of 4.6σ noise level in the Band 7 data at the position of CO(2–1) line which is the same as the detection limit in § 2.2.

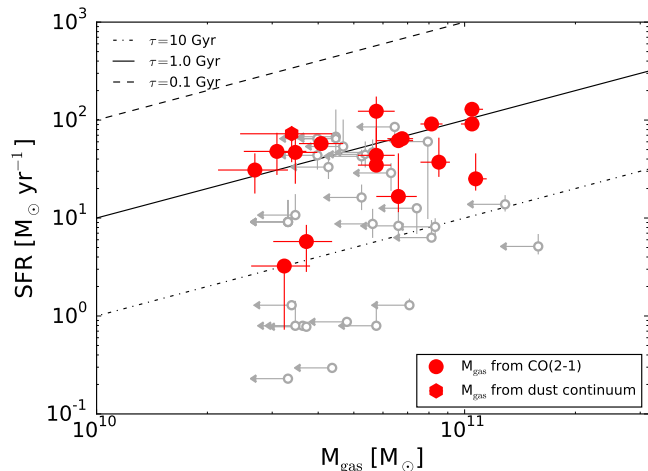


FIG. 6.— SFRs as a function of molecular gas mass. The red circles are 17 CO(2–1) emitters and the red hexagon is the dust continuum source. The gray symbols show the upper limit of molecular gas at the SFR estimated. The dash-dotted, solid, and dashed lines show a constant depletion time scale, $\text{SFR}/M_{\text{gas}}$, of 0.1, 1.0, and 10 Gyr, respectively.

The former two factors are related with the properties of galaxies themselves. Stellar mass of galaxies is one of the most important properties showing the tight correlation with other galaxy properties such as star formation, metallicity, and size. The offset of the MS is also an important factor to discuss the relation between the gas reservoirs and star formation activity in cluster galaxies. On the other hand, the latter two factors should

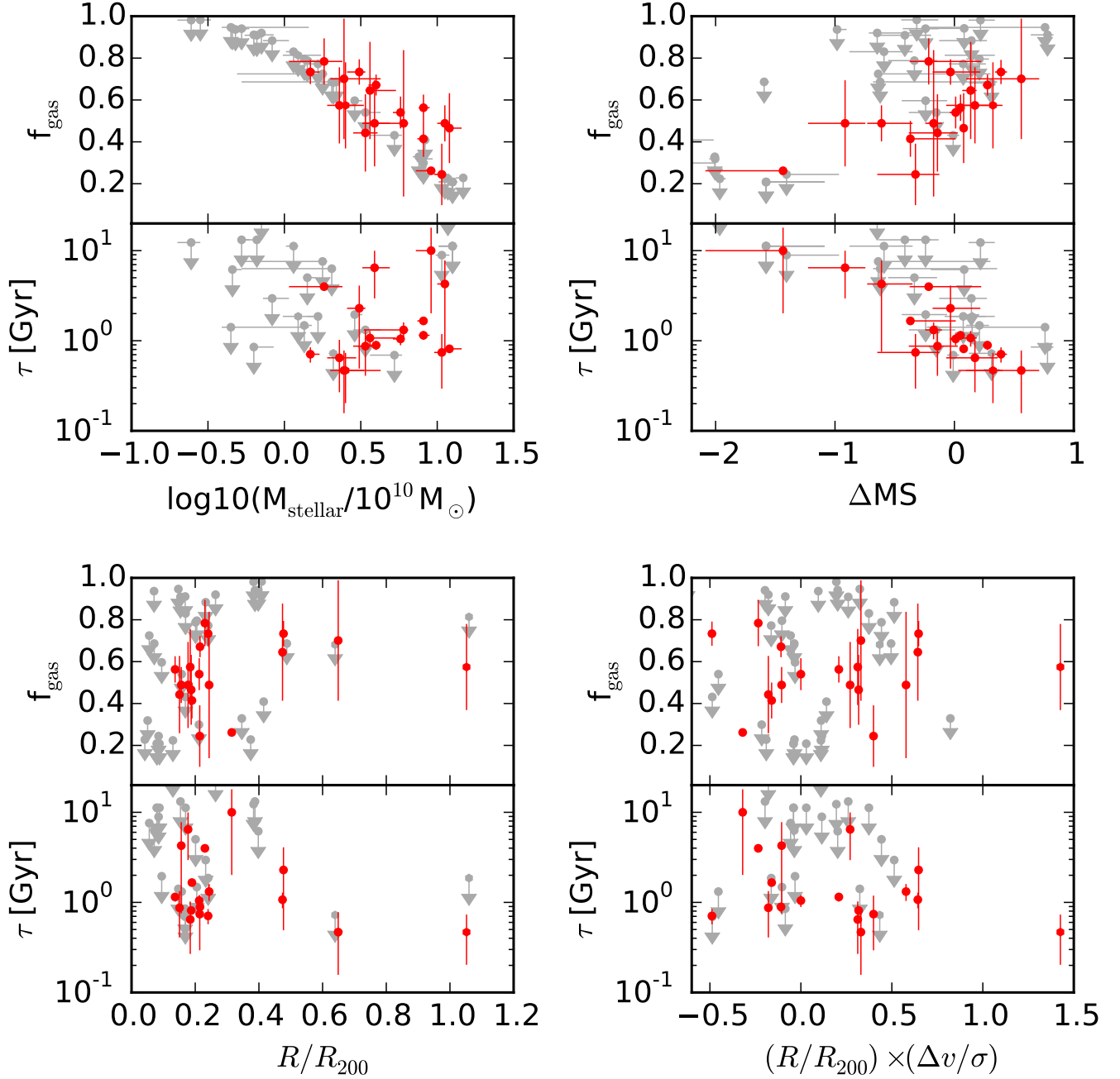


FIG. 7.— Molecular gas fraction, $f_{\text{gas}} = M_{\text{gas}}/(M_{\text{gas}} + M_{\text{stellar}})$, and depletion time, $\tau = M_{\text{gas}}/\text{SFR}$, of the cluster member galaxies as a function of stellar mass (M_{stellar}), offset from the main sequence (ΔMS), cluster-centric radius (R/R_{200}), and accretion phase ($(R/R_{200}) \times (\Delta v/\sigma)$), where we assume the MS of star-forming galaxies at $z = 1.46$ given by [Speagle et al. \(2014\)](#). The red symbols show the 18 ALMA sources detected in CO(2–1) or dust continuum. The gray symbols show the upper limit of gas fraction and depletion time for the other member galaxies without detection in ALMA data.

give us insight into evolutionary processes peculiar to galaxy clusters after they belong to the galaxy cluster. A phase-space diagram is a useful tool to characterize the accretion state of cluster member galaxies relatively free from effects due to the 2D projected positions with respect to the cluster center ([Noble et al. 2013, 2016](#); [Jaffé et al. 2015](#); [Muzzin et al. 2014](#)). [Hayashi et al. \(2017\)](#) show that the CO emitters tend to be distributed at the edge of the virialized region or in the region of relatively recent accretion. The galaxies with CO line detected dis-

appear from the very center of the cluster. They argue that the gas-rich galaxies with CO detections have spent only relatively short times within the cluster.

Figure 7 shows gas fraction (f_{gas}) and depletion time (τ) of the 18 gas-rich member galaxies as a function of stellar mass, offset from the MS, cluster-centric radius, and accretion phase, respectively. We assume the MS of star-forming galaxies at $z = 1.46$ given by [Speagle et al. \(2014\)](#) which investigate the evolution of MS up to $z \sim 6$ by compiling 25 studies from the literature. The offset of

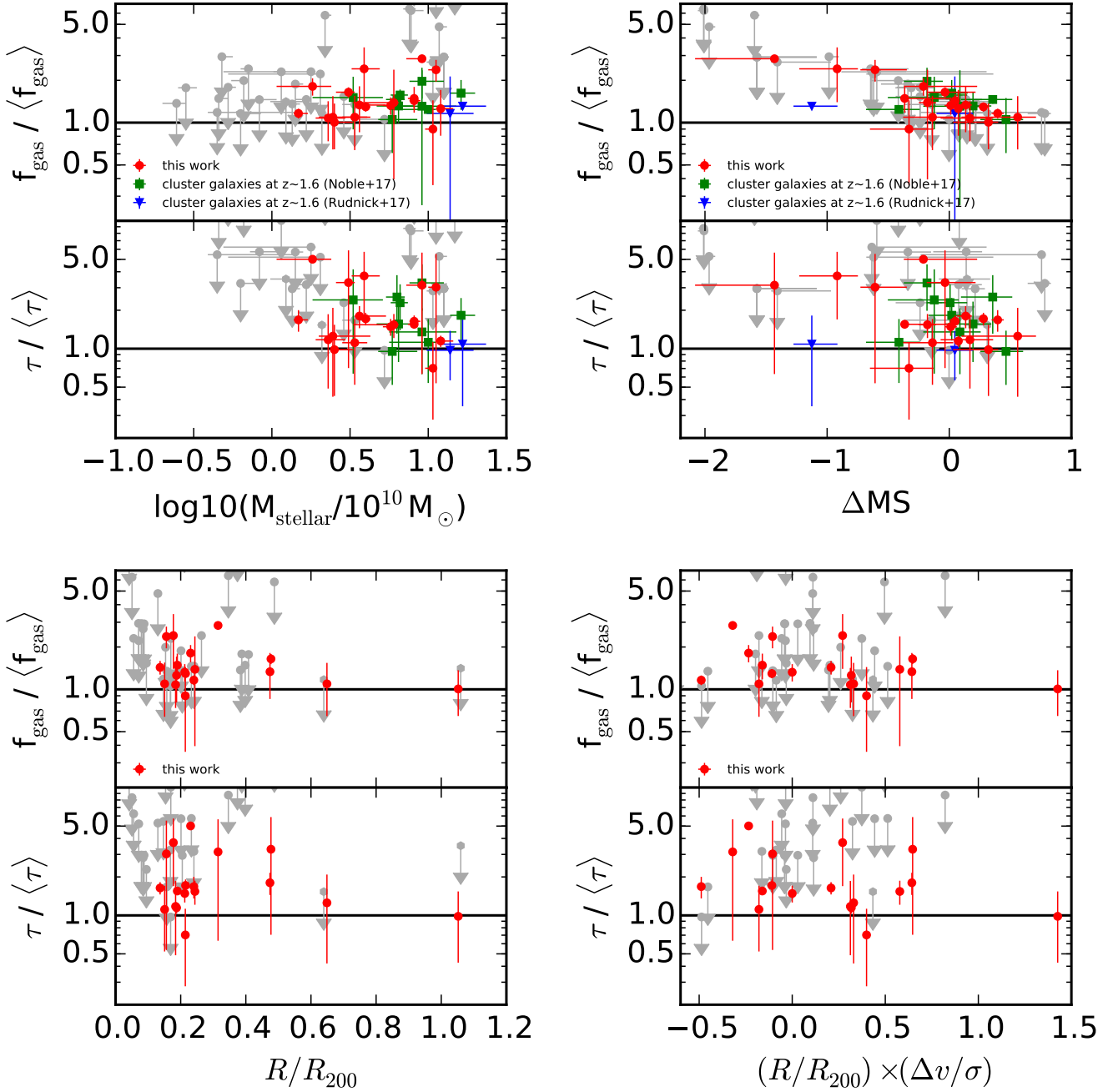


FIG. 8.— Same as Figure 7, but the gas fraction and the depletion time are compared with what is expected from the scaling relations for field galaxies given by Tacconi et al. (2018). The main sequence is derived from the literature of Speagle et al. (2014). The scaling relations are functions of redshift, stellar mass, and ratio of specific SFR to that of MS galaxies with a given stellar mass at the redshift, and thus take account of the redshift evolution of specific SFR. The horizontal line in each panel shows the gas fraction and the depletion time on the scaling relations. The red circles show our results. The green squares show the results of Noble et al. (2017) for galaxies in three galaxy clusters at $z \sim 1.6$ and the blue triangles show the results of Rudnick et al. (2017) for galaxies in a galaxy cluster at $z \sim 1.6$.

the MS is derived from a difference between the SFR and the expectation from the MS at a given stellar mass. We also plot the upper limits of gas fraction and depletion time for the other member galaxies.

The gas fractions in the massive galaxies with $M_{\text{stellar}} \sim 10^{11} M_{\odot}$ are roughly less than half and the depletion time scale is $\gtrsim 1$ Gyr. In particular, these galaxies with $\Delta MS < -1$ show lower gas fraction of $< 1/3$, suggesting that massive quiescent galaxies no longer have

large gas reservoir and efficient star formation in the cluster center. On the other hand, the galaxies above the MS show larger gas fraction and smaller depletion time scale as the offset from the MS is larger. The galaxies with larger offset from the MS tend to be gas-rich galaxies forming stars in starburst phase. As long as we focus on the galaxies with CO and dust continuum detected, most of them show $f_{\text{gas}} \gtrsim 0.4$ and $\tau \gtrsim 1$ Gyr and there is no strong dependence of gas fraction and depletion time on

the cluster-centric radius and the accretion phase. However, it is also a fact that massive quiescent galaxies that show $f_{\text{gas}} \lesssim 0.2$ and $\tau \sim 10$ Gyr exist in the cluster center. These are few member galaxies with an intermediate gas fraction and depletion time scale. Some rapid processes may be able to reduce the gas reservoirs in cluster galaxies.

We integrate the molecular gas mass, stellar mass and SFR for the member galaxies within a radius of $0.5R_{200}$ to estimate an average gas fraction, $\langle f_{\text{gas}} \rangle = \sum M_{\text{gas}} / \sum M_{\text{stellar}}$, and an average depletion time scale, $\langle \tau \rangle = \sum M_{\text{gas}} / \sum \text{SFR}$, in the cluster. The gas fraction and depletion time ranges $\langle f_{\text{gas}} \rangle = 0.29\text{--}0.53$ and $\langle \tau \rangle = 0.83\text{--}2.3$ Gyr, where the upper limit is derived by taking account of the upper limit of gas mass for the member galaxies without ALMA detection and the lower limit is derived by assuming no gas mass for these member galaxies.

4. DISCUSSION

4.1. Comparison with the scaling relations

Scaling relations of gas to stellar mass ratio ($M_{\text{gas}}/M_{\text{stellar}}$) and depletion time scale on both specific SFR and its offset from the MS are derived by Tacconi et al. (2018) from the compilation of more than one thousand measurements of molecular gas mass for galaxies at $z = 0\text{--}4$ with a wide range of stellar mass and SFR. We use the scaling relations to compare our results with the representative populations in general fields at similar redshifts, where we assume the MS of Speagle et al. (2014) as in Tacconi et al. (2018). Figure 8 shows the ratio of molecular gas fraction and depletion time to what is expected from the scaling relations as a function of stellar mass, offset from the MS, cluster-centric radius, and accretion phase based on phase space.

The member galaxies with CO and/or dust continuum detected in the cluster tend to have larger gas fraction and larger depletion time, compared with those from the scaling relations. The cluster galaxies with large offset below from the MS also have the gas fraction larger than that for field galaxies, nevertheless they are quenching star formation. Judging from the distribution of the cluster galaxies in the SFR- M_{stellar} diagram (Figure 3), the larger depletion time scale is due not to the lower SFR but to the larger amount of gas. The results may imply that the infalling regions and filaments around galaxy clusters are easier to feed gas to member galaxies, which results in the larger gas fraction in cluster galaxies. Also, some environmental effects peculiar to galaxies associated with galaxy clusters may reduce the efficiency of star formation. We speculate that the shock-heating by ram pressure can be one of the causes of the low efficiency (Jáchym et al. 2014; Wong et al. 2014). Although the statistics is poor, it seems that the member galaxies in $R \gtrsim 0.5R_{200}$ or with phases accreting more recently have gas fraction and depletion time consistent with the scaling relations. On the other hand, the member galaxies infalling to closer to the cluster center can have larger gas fraction and larger depletion time than the scaling relations. This supports that some environmental effects have impacted the galaxies while moving within the galaxy cluster. Moreover, if the negative feedback from active galactic nucleus (AGN) and/or super-

nova (SN) works on the galaxies (Carniani et al. 2017), the efficiency of star formation would be further reduced, although some studies suggests the possibility of the positive feedback by AGNs (Kakkad et al. 2017).

However, we cannot completely exclude the possibility that we overestimate the molecular gas mass. Although we use a conversion factor, α_{CO} , dependent on stellar mass (i.e., metallicity through the mass-metallicity relation), if the cluster galaxies have higher metallicity at a given stellar mass, then the actual conversion factor should be smaller than what we apply in this work. This can result in the overestimation of molecular mass by a factor of ~ 1.5 , based on the conversion factors that we apply in § 3.1. The mass-metallicity relation in galaxy clusters at high redshifts is still controversial, however, several studies suggest that less massive galaxies in high- z galaxy clusters tend to be more metal-rich than the field galaxies, while massive galaxies do not show such a difference between galaxy clusters and fields (Kulas et al. 2013; Shimakawa et al. 2015).

4.2. Comparison with other clusters at similar redshifts

To discuss how representative the results that we have found are in galaxy clusters at $z \sim 1.5$, we compare with two studies in galaxy clusters at $z \sim 1.6$ (Noble et al. 2017; Rudnick et al. 2017). Noble et al. (2017) have detected CO (2-1) emission lines from 11 gas-rich galaxies in three galaxy clusters at $z \sim 1.6$ using ALMA. They argue that the cluster galaxies tend to have enhanced gas fractions compared with the field scaling relations at $z = 1.6$ but they have depletion timescales consistent with the field galaxies. These three clusters are found by the Spitzer Adaptation of the Red-Sequence Cluster Survey (SpARCS; Wilson et al. 2009; Muzzin et al. 2009). They estimate the cluster mass of $\gtrsim 10^{14} M_{\odot}$ from the richness of member galaxies (Noble et al. 2017). Rudnick et al. (2017) have detected CO(1-0) emission lines from two massive galaxies in a confirmed $z = 1.62$ galaxy cluster (Papovich et al. 2010; Tanaka et al. 2010) using the Karl G. Jansky Very Large Array (VLA). They argue that the gas fractions and star formation efficiencies of the galaxies in the cluster are comparable to the field galaxy scaling relations. The cluster mass is estimated to be $1.1 \times 10^{14} M_{\odot}$ from XMM-Newton X-ray data (Papovich et al. 2010; Tanaka et al. 2010). Because the cluster mass of the XMMXCS J2215.9-1738 cluster is estimated to be $\sim 3 \times 10^{14} M_{\odot}$, all of these clusters are systems with similar mass scale.

The molecular masses for the galaxies associated with the galaxy clusters at $z \sim 1.6$ are derived in the same manner as in Section 3.1 using the information available from the literature (Noble et al. 2017; Rudnick et al. 2017) for proper comparison with our results. We use the stellar masses and SFRs of the galaxies shown in the literature. The comparison with the results in the galaxy clusters at $z \sim 1.6$ show that our results are consistent with the other clusters at similar redshifts (Figure 8). Therefore, we conclude that cluster galaxies at $z \sim 1.5$ can have the molecular gas fraction larger than what the field galaxies have. While the depletion time scale of the massive cluster galaxies with $\sim 10^{11} M_{\odot}$ are similar to the field galaxies, less massive galaxies can have larger depletion time.

TABLE 3
AVERAGE PROPERTIES OF THE CONFIRMED MEMBER GALAXIES WITHIN A HALF OF R_{200} OBTAINED FROM STACKED SPECTRA IN BAND 3

	Number ^a	$\langle M_{\text{stellar}} \rangle^b$ ($10^{10} M_{\odot}$)	$\langle \text{SFR} \rangle^b$ ($M_{\odot} \text{ yr}^{-1}$)	$S\Delta v^c$ (Jy km s^{-1})	$M_{\text{gas, CO}}$ ($10^{10} M_{\odot}$)	f_{gas}	τ (Gyr)
Quiescent	12 (1)	11.0	1	<0.07	<0.93	<0.08	<9.78
Star-forming	27 (15)	2.3	31	0.21	3.83	0.63	1.24
Star-forming w/o CO	12 (0)	0.6	7	<0.04	<1.05	<0.62	<1.58

^a The number of galaxies stacked. The values within parentheses are the number of galaxies with CO(2–1) detected individually.

^b The median values in the samples.

^c Estimated from the intensity map integrated in velocity by 400 km s^{-1} .

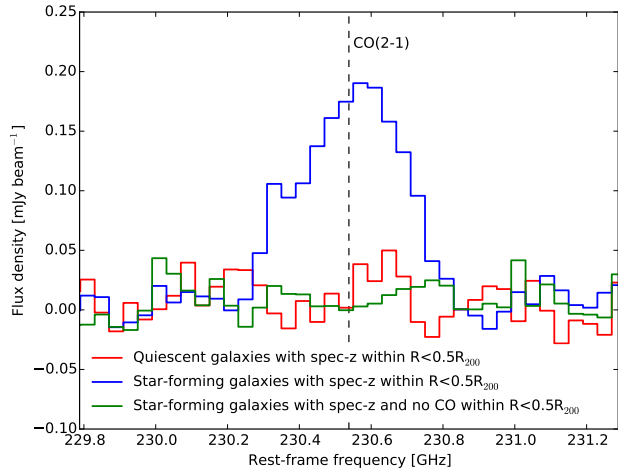


FIG. 9.— Stacked spectra around $\nu_{\text{rest}} = 230.538 \text{ GHz}$ in ALMA Band 3 data for quiescent galaxies (red), star-forming galaxies (blue), and star-forming galaxies without CO detected individually (green) that are spectroscopically confirmed within a radius of $0.5R_{200}$. The dashed line shows a frequency of CO(2–1) emission line. The quiescent or star-forming galaxies are classified by the U-V and V-J color diagram (Figure 4). The CO(2–1) emission line is not detected from the stacked spectrum of quiescent galaxies. The flux or the upper limit of flux of the emission line in the stacked spectrum is shown in Table 3.

4.3. Molecular gas reservoirs of quiescent galaxies

The member galaxies with CO line and/or dust continuum detected are located away from the very center of the cluster (Figure 1). It is worth investigating how much the gas reservoirs of the member galaxies in the very center is left. To give a constraint on molecular gas mass for such galaxies, the stacked data in the Band 3 are used to discuss the average amount of the molecular gas in these member galaxies.

We stack the Band 3 data for two populations of quiescent galaxies and star-forming galaxies which are classified based on the UVJ diagram (Figure 4). There are 12 quiescent galaxies and 27 star-forming galaxies that are spectroscopically confirmed within a half of R_{200} . Among them, a quiescent galaxy and 15 star-forming galaxies have CO(2–1) line detected. The redshift confirmation is essential to shift the individual spectrum from the observed-frame to the rest-frame. Figure 9 shows the stacked spectra for three samples from the two populations; all quiescent galaxies, all star-forming galaxies, and star-forming galaxies without CO(2–1) detection. For the sample of all star-forming galaxies, since

about a half of them have CO(2–1) lines detected individually, the CO(2–1) line is also detected in the stacked spectrum. On the other hand, the stacked spectra of the quiescent galaxies and star-forming galaxies without CO detected individually show no detection of CO(2–1) line. Using the intensity map integrated in velocity by 400 km s^{-1} , the average CO(2–1) line flux and the 5σ upper limit flux are estimated for the star-forming and quiescent galaxies, respectively. We then convert them to the molecular gas masses in the same manner as in § 3.1. Note that we make sure the validity of our procedure by stacking the data for the member galaxies with CO(2–1) detected individually. The measurements from the stacked spectra are shown in Table 3.

The upper limit of molecular gas for the quiescent galaxies shows the gas fraction of < 0.08 and the depletion time scale of $< 9.8 \text{ Gyr}$, suggesting that the quiescent galaxies in the center consume most of their molecular gas. On the other hand, star-forming galaxies still have enough gas to keep forming stars. However, many star-forming galaxies in the cluster have larger gas reservoirs compared with the field galaxies (§ 4.1), and they also show the larger depletion time as they deviate from the MS. This may imply that it is difficult to consume the molecular gas by only star formation. The starvation to stop supply gas to the cluster galaxies as well as the ram-pressure to strip gas from the galaxies may be required to effectively reduce the amount of the molecular gas, which can accelerate the growth of cluster galaxies to become quiescent galaxies in the cluster core. Indeed, it is observed that the molecular gas as well as HI gas are stripped from galaxies by ram pressure in the local galaxy cluster (Sivanandam et al. 2010; Jáchym et al. 2014). Also, virial shock in the massive halo of this cluster at $z = 1.46$ would prevent the cold gas stream from accreting to the member galaxies settled in the cluster center (Birnboim & Dekel 2003; Dekel & Birnboim 2006). Other possibility is galaxy mergers. The merging of gas-rich galaxies can induce starburst in the galaxy center (Hopkins et al. 2008), which results in consumption of gas reservoirs. The stellar masses of the gas-rich galaxies in this cluster are comparable to and/or a factor of ~ 2 – 5 smaller than those of quiescent galaxies. A perspective of mass growth supports that the merging is one of possible processes. The feedback from AGN and SN can also have a role in the quenching mechanism. Outflows of massive molecular gas by AGNs and SNe are observed from ultraluminous infrared galaxies (ULIRGs) in the local Universe (Feruglio et al. 2010; Sturm et al. 2011; Ciccone et al. 2014). Since there is no evidence that a high fraction of the starburst galaxies and AGNs are

found in this cluster, the feedback may be an inadequate process for environmental effects to the transition of star-forming galaxies to quiescent galaxies in galaxy clusters, however it would be one of the important processes not only to reduce the efficiency of star formation but also to blow the gas off from the galaxies.

There are a few previous studies to show a constraint on molecular gas fraction for quiescent galaxies at similar redshifts. Sargent et al. (2015) present the upper limit of CO(2–1) luminosity in an early-type galaxies at $z = 1.43$ with IRAM/Plateau de Bure Interferometer (PdBI), which shows the 3σ upper limit of gas fraction is $\lesssim 10\%$. Gobat et al. (2017) use the stacked SED ranging from MIR to radio for about thousand early-type galaxies at $\langle z \rangle = 1.76$ to give a constraint on their molecular gas reservoirs. The gas mass is derived from the dust mass that is estimated from the SED under the assumption of a metallicity-dependent gas-to-dust ratio. They derive the gas fraction of $\sim 13\%$. Note that the stellar masses shown in the literature is converted to that with Chabrier (2003) IMF. The gas fraction that we derive for the quiescent galaxies in the galaxy cluster at $z = 1.46$ is similar to those for the field quiescent galaxies at similar redshifts, suggesting that quiescent galaxies consume the fuel of gas down to similar low level of $\lesssim 10\%$ irrespective of the environment. However, The ATLAS^{3D} project shows that the early-type galaxies in the local Universe have a gas fraction an order of magnitude smaller than that for the galaxies at $z \sim 1.5$ (Young et al. 2011). Preferably, the local post-starburst galaxies seem to have a gas fraction similar to the high- z cluster quiescent galaxies (French et al. 2015).

5. SUMMARY AND CONCLUSIONS

We conduct the ALMA observations in Band 3 and Band 7 in the X-ray galaxy cluster, XMMXCS J2215.9-1738, at $z = 1.46$. While the Band 3 data allow us to detect CO(2–1) emission lines from cluster member galaxies, the Band 7 data allow us to detect dust continuum emissions at $870 \mu\text{m}$. We use these ALMA data to investigate molecular gas reservoirs in the member galaxies within a cluster-centric radius of $\sim R_{200}$ and then discuss the evolution of their star formation activities in terms of star formation efficiency and gas consumption.

Hayashi et al. (2017) already report the discovery of 17 CO(2–1) emission lines associated with the cluster. In this paper, we newly detect nine $870 \mu\text{m}$ sources in the Band 7 data. Although one source is a foreground galaxy, the other eight galaxies are confirmed to be cluster member galaxies. Seven galaxies have both CO(2–1) lines and dust continuum emissions detected, and the position of dust continuum emission is consistent with that of CO(2–1) emission. Consequently, we have CO(2–1) emission lines and/or dust continuum emissions from 18 member galaxies within $\sim R_{200}$. The rest-frame U-V versus V-J color diagram shows that most of the CO lines and/or dust emissions are detected from dusty star-forming galaxies.

We derive molecular gas masses from the CO luminosities using the metallicity-dependent (i.e., stellar mass-dependent) conversion factors (Tacconi et al. 2018) as well as dust continuum luminosities according to Scoville et al. (2016) while taking into account of the metallicity-dependency of the dust-to-gas ratio. The molecular gas

masses derived from the two ways are consistent with each other.

We investigate the gas fraction and the depletion time scale as a function of stellar mass, offset from the main sequence of star-forming galaxies, cluster-centric radius, and accretion phase. The galaxies with larger SFRs at a given stellar mass show a larger gas fraction and a smaller depletion time scale. There is no strong dependence of gas fraction and depletion time on the cluster-centric radius and the accretion phase. The cluster member galaxies with CO and/or dust continuum detected tend to have a larger gas fraction and a larger depletion time, compared with those from the scaling relations for field galaxies. If infalling regions and filaments around galaxy clusters help feed the gas through inflow to member galaxies, the cluster galaxies can have the larger gas reservoirs than the field galaxies at $z \sim 1.5$. Nevertheless, the cluster galaxies must become more inefficient in star formation than field galaxies. As the member galaxies are infalling to closer to the center, the deviation of gas fraction and depletion time from the scaling relations seems to get larger. Therefore, some environmental effects peculiar to galaxies associated with galaxy clusters may reduce the efficiency of star formation.

Massive quiescent galaxies in the cluster core no longer have large gas reservoirs and efficient star formation. We stack the Band 3 spectra for 12 quiescent galaxies within a radius of $0.5 R_{200}$. However, no CO(2–1) emission line is detected from the stacked spectrum. The upper limits of molecular gas and molecular gas fraction are estimated to be $\lesssim 10^{10} M_{\odot}$ and $\lesssim 10\%$, respectively, which are similar to those for quiescent galaxies in general fields at similar redshifts. This suggests that irrespective of the environment, the massive quiescent galaxies consume most of the fuel of gas and evolve passively in the center of the cluster. We speculate that since cluster member galaxies are subject to additional environmental effects such as ram-pressure, starvation, and merging compared with field galaxies, cluster galaxies is easier to reduce gas reservoirs and then quench star formation, which results in a larger fraction of quiescent galaxies in galaxy clusters rather than in general fields.

We thank the anonymous referee for providing constructive comments and suggestions. MH acknowledges the financial support by JSPS Grant-in-Aid for Young Scientists (A) Grant Number JP26707006 and was also supported by the ALMA Japan Research Grant of NAOJ Chile Observatory, NAOJ-ALMA-180. KK acknowledges the financial support by the JSPS Grant-in-Aid for Scientific Research (A) JP25247019. YY is thankful for the JSPS fellowship. This paper makes use of the following ALMA data: ADS/JAO.ALMA#2011.1.00623.S and ADS/JAO.ALMA#2015.1.00779.S. ALMA is a partnership of ESO, NSF (USA) and NINS (Japan), together with NRC (Canada), NSC and ASIAA (Taiwan), and KASI (Republic of Korea), in cooperation with the Republic of Chile. The Joint ALMA Observatory is operated by ESO, AUI/NRAO and NAOJ. This work uses the data collected at Subaru Telescope, which is operated by the National Astronomical Observatory of Japan. This work also uses the data based on observations obtained with MegaPrime/MegaCam, a joint project of

CFHT and CEA/IRFU, at the Canada-France-Hawaii Telescope (CFHT) which is operated by the National Research Council (NRC) of Canada, the Institut National des Science de l'Univers of the Centre National de la Recherche Scientifique (CNRS) of France, and the University of Hawaii. This work is based in part on data products produced at Terapix available at the Canadian Astronomy Data Centre as part of the Canada-France-Hawaii Telescope Legacy Survey, a collaborative project

of NRC and CNRS. Some of the data presented in this paper were obtained from the Mikulski Archive for Space Telescopes (MAST). STScI is operated by the Association of Universities for Research in Astronomy, Inc., under NASA contract NAS5-26555. Support for MAST for non-HST data is provided by the NASA Office of Space Science via grant NNX09AF08G and by other grants and contracts

Facilities: ALMA, Subaru, CFHT, HST.

REFERENCES

- Aravena, M., et al. 2012, *MNRAS*, 426, 258
 Barro, G., et al. 2016, *ApJ*, 827, L32
 Beifiori, A., et al. 2017, *ApJ*, 846, 120
 Bertin, E., & Arnouts, S. 1996, *A&AS*, 117, 393
 Bielby, R., et al. 2012, *A&A*, 545, A23
 Birnboim, Y., & Dekel, A. 2003, *MNRAS*, 345, 349
 Bolatto, A. D., Wolfire, M., & Leroy, A. K. 2013, *ARA&A*, 51, 207
 Brammer, G. B., et al. 2011, *ApJ*, 739, 24
 Bruzual, G., & Charlot, S. 2003, *MNRAS*, 344, 1000
 Calzetti, D., Armus, L., Bohlin, R. C., Kinney, A. L., Koornneef, J., & Storchi-Bergmann, T. 2000, *ApJ*, 533, 682
 Cardelli, J. A., Clayton, G. C., & Mathis, J. S. 1989, *ApJ*, 345, 245
 Carilli, C. L., & Walter, F. 2013, *ARA&A*, 51, 105
 Carniani, S., et al. 2017, *A&A*, 605, A105
 Casasola, V., Magrini, L., Combes, F., Mignano, A., Sani, E., Paladino, R., & Fontani, F. 2013, *A&A*, 558, A60
 Chabrier, G. 2003, *PASP*, 115, 763
 Chapman, S. C., et al. 2015, *MNRAS*, 449, L68
 Chen, C.-C., et al. 2017, *ApJ*, 846, 108
 Cicone, C., et al. 2014, *A&A*, 562, A21
 Daddi, E., et al. 2007, *ApJ*, 670, 156
 Dannerbauer, H., et al. 2017, *A&A*, 608, A48
 Decarli, R., et al. 2016a, *ApJ*, 833, 69
 Decarli, R., et al. 2016b, *ApJ*, 833, 70
 Dekel, A., & Birnboim, Y. 2006, *MNRAS*, 368, 2
 Dressler, A., et al. 1997, *ApJ*, 490, 577
 Elbaz, D., et al. 2007, *A&A*, 468, 33
 Feruglio, C., Maiolino, R., Piconcelli, E., Menci, N., Aussel, H., Lamastra, A., & Fiore, F. 2010, *A&A*, 518, L155
 French, K. D., Yang, Y., Zabludoff, A., Narayanan, D., Shirley, Y., Walter, F., Smith, J.-D., & Tremonti, C. A. 2015, *ApJ*, 801, 1
 Fujimoto, S., Ouchi, M., Ono, Y., Shibuya, T., Ishigaki, M., Nagai, H., & Momose, R. 2016, *ApJS*, 222, 1
 Geach, J. E., Smail, I., Moran, S. M., MacArthur, L. A., Lagos, C. d. P., & Edge, A. C. 2011, *ApJ*, 730, L19
 Genzel, R., et al. 2012, *ApJ*, 746, 69
 Genzel, R., et al. 2015, *ApJ*, 800, 20
 Gobat, R., et al. 2017, arXiv:1703.02207
 Hatsukade, B., et al. 2016, *PASJ*, 68, 36
 Hayashi, M., Kodama, T., Koyama, Y., Tadaki, K.-i., & Tanaka, I. 2011, *MNRAS*, 415, 2670
 Hayashi, M., Kodama, T., Koyama, Y., Tanaka, I., Shimasaku, K., & Okamura, S. 2010, *MNRAS*, 402, 1980
 Hayashi, M., et al. 2014, *MNRAS*, 439, 2571
 Hayashi, M., et al. 2017, *ApJ*, 841, L21
 Hilton, M., et al. 2010, *ApJ*, 718, 133
 Hodge, J. A., et al. 2016, *ApJ*, 833, 103
 Hopkins, P. F., Hernquist, L., Cox, T. J., & Kereš, D. 2008, *ApJS*, 175, 356
 Ikarashi, S., et al. 2015, *ApJ*, 810, 133
 Ivison, R. J., et al. 2013, *ApJ*, 772, 137
 Jáchym, P., Combes, F., Cortese, L., Sun, M., & Kenney, J. D. P. 2014, *ApJ*, 792, 11
 Jaffé, Y. L., Smith, R., Candlish, G. N., Poggianti, B. M., Sheen, Y.-K., & Verheijen, M. A. W. 2015, *MNRAS*, 448, 1715
 Kakkad, D., et al. 2017, *MNRAS*, 468, 4205
 Kennicutt, R. C., & Evans, N. J. 2012, *ARA&A*, 50, 531
 Kennicutt, Jr., R. C. 1998, *ApJ*, 498, 541
 Koyama, S., et al. 2017, *ApJ*, 847, 137
 Koyama, Y., et al. 2013, *MNRAS*, 434, 423
 Kriek, M., van Dokkum, P. G., Labbé, I., Franx, M., Illingworth, G. D., Marchesini, D., & Quadri, R. F. 2009, *ApJ*, 700, 221
 Kulas, K. R., et al. 2013, *ApJ*, 774, 130
 Labbé, I., et al. 2005, *ApJ*, 624, L81
 Lee, M. M., et al. 2017, *ApJ*, 842, 55
 Ma, C.-J., et al. 2015, *ApJ*, 806, 257
 Madau, P., & Dickinson, M. 2014, *ARA&A*, 52, 415
 Magnelli, B., Elbaz, D., Chary, R. R., Dickinson, M., Le Borgne, D., Frayer, D. T., & Willmer, C. N. A. 2009, *A&A*, 496, 57
 Magnelli, B., et al. 2012, *A&A*, 548, A22
 Maiz Apellániz, J. 2006, *AJ*, 131, 1184
 McMullin, J. P., Waters, B., Schiebel, D., Young, W., & Golap, K. 2007, in *Astronomical Society of the Pacific Conference Series*, Vol. 376, *Astronomical Data Analysis Software and Systems XVI*, ed. R. A. Shaw, F. Hill, & D. J. Bell, 127
 Muzzin, A., et al. 2009, *ApJ*, 698, 1934
 Muzzin, A., et al. 2014, *ApJ*, 796, 65
 Noble, A. G., Webb, T. M. A., Muzzin, A., Wilson, G., Yee, H. K. C., & van der Burg, R. F. J. 2013, *ApJ*, 768, 118
 Noble, A. G., Webb, T. M. A., Yee, H. K. C., Muzzin, A., Wilson, G., van der Burg, R. F. J., Balogh, M. L., & Shupe, D. L. 2016, *ApJ*, 816, 48
 Noble, A. G., et al. 2017, *ApJ*, 842, L21
 Noeske, K. G., et al. 2007, *ApJ*, 660, L43
 Papovich, C., et al. 2010, *ApJ*, 716, 1503
 Peng, Y.-j., et al. 2010, *ApJ*, 721, 193
 Renzini, A., & Peng, Y.-j. 2015, *ApJ*, 801, L29
 Rudnick, G., et al. 2017, *ApJ*, 849, 27
 Saintonge, A., et al. 2012, *ApJ*, 758, 73
 Saintonge, A., et al. 2013, *ApJ*, 778, 2
 Saintonge, A., et al. 2016, *MNRAS*, 462, 1749
 Saintonge, A., et al. 2017, *ApJS*, 233, 22
 Sargent, M. T., et al. 2014, *ApJ*, 793, 19
 Sargent, M. T., et al. 2015, *ApJ*, 806, L20
 Schmidt, M. 1959, *ApJ*, 129, 243
 Schreiber, C., et al. 2015, *A&A*, 575, A74
 Scoville, N., et al. 2013, *ApJS*, 206, 3
 Scoville, N., et al. 2016, *ApJ*, 820, 83
 Scoville, N., et al. 2017, *ApJ*, 837, 150
 Seko, A., Ohta, K., Yabe, K., Hatsukade, B., Akiyama, M., Iwamura, F., Tamura, N., & Dalton, G. 2016, *ApJ*, 819, 82
 Shimakawa, R., Kodama, T., Tadaki, K.-i., Hayashi, M., Koyama, Y., & Tanaka, I. 2015, *MNRAS*, 448, 666
 Silverman, J. D., et al. 2015, *ApJ*, 812, L23
 Simpson, J. M., et al. 2015, *ApJ*, 807, 128
 Sivanandam, S., Rieke, M. J., & Rieke, G. H. 2010, *ApJ*, 717, 147
 Sobral, D., Stroe, A., Koyama, Y., Darvish, B., Calhau, J., Afonso, A., Kodama, T., & Nakata, F. 2016, *MNRAS*, 458, 3443
 Speagle, J. S., Steinhardt, C. L., Capak, P. L., & Silverman, J. D. 2014, *ApJS*, 214, 15
 Stach, S. M., Swinbank, A. M., Smail, I., Hilton, M., Simpson, J. M., & Cooke, E. A. 2017, *ApJ*, 849, 154
 Stanford, S. A., et al. 2006, *ApJL*, 646, L13
 Sturm, E., et al. 2011, *ApJ*, 733, L16
 Tacconi, L. J., et al. 2010, *Nature*, 463, 781
 Tacconi, L. J., et al. 2013, *ApJ*, 768, 74
 Tacconi, L. J., et al. 2018, *ApJ*, 853, 179
 Tadaki, K.-i., et al. 2014, *ApJ*, 788, L23
 Tadaki, K.-i., et al. 2015, *ApJ*, 811, L3
 Tadaki, K.-i., et al. 2017, *ApJ*, 834, 135
 Tanaka, M., Finoguenov, A., & Ueda, Y. 2010, *ApJL*, 716, L152
 Wagg, J., et al. 2012, *ApJ*, 752, 91
 Walter, F., et al. 2014, *ApJ*, 782, 79
 Wang, T., et al. 2016, *ApJ*, 828, 56
 Webb, T. M. A., et al. 2017, *ApJ*, 844, L17
 Whitaker, K. E., Pope, A., Cybulski, R., Casey, C. M., Popping, G., & Yun, M. S. 2017, *ApJ*, 850, 208
 Whitaker, K. E., et al. 2014, *ApJ*, 795, 104
 Williams, J. P., de Geus, E. J., & Blitz, L. 1994, *ApJ*, 428, 693
 Williams, R. J., Quadri, R. F., Franx, M., van Dokkum, P., & Labbé, I. 2009, *ApJ*, 691, 1879
 Wilson, G., et al. 2009, *ApJ*, 698, 1943
 Wong, O. I., Kenney, J. D. P., Murphy, E. J., & Helou, G. 2014, *ApJ*, 783, 109
 Wuyts, S., Labbé, I., Förster Schreiber, N. M., Franx, M., Rudnick, G., Brammer, G. B., & van Dokkum, P. G. 2008, *ApJ*, 682, 985
 Wuyts, S., et al. 2011, *ApJ*, 738, 106
 Young, L. M., et al. 2011, *MNRAS*, 414, 940